High average output power from a backside-cooled 2-μm InGaSb VECSEL with full gain characterization

MARCO GAULKE,[1,*] JONAS HEIDRICH,[1] B. ÖZGÜR ALAYDIN,[1,2] MATTHIAS GOLLING,[1] AJANTA BARH,[1] AND URSULA KELLER[1]

[1]*ETH Zurich, Department of Physics, Institute for Quantum Electronics, Auguste-Piccard-Hof 1, Zurich 8093, Switzerland*
[2]*Current address: Sivas Cumhuriyet University Department of Physics, Turkey*
gaulkem@ethz.ch

Abstract: We compare the gain and continuous wave lasing properties of two InGaSb-based vertical external cavity surface emitting lasers (InGaSb VECSEL) with different heat management approaches operating at a center wavelength of around 2 μm. To date, intracavity heatspreaders have been required for good average output power, which have many trade-offs, especially for passive modelocking. Here we demonstrate a record high average output power of 810 mW without an intracavity heatspreader using a backside-cooled non-resonant VECSEL chip optimized for modelocking. In addition, we introduce and demonstrate an optical characterization for a wavelength range of 1.9 to 3 μm to precisely measure wavelength-dependent gain saturation and spectral gain. Gain characteristics are measured as a function of wavelength, fluence, pump power and temperature. Small signal gain of more than 5%, small saturation fluences and broad gain bandwidths of more than 90 nm are demonstrated. In comparison to a commercial VECSEL chip with an intracavity heatspreader, we have obtained similar average output power even though our VECSEL chip is designed for antiresonance.

1. Introduction

Optically pumped vertical external cavity surface emitting lasers (VECSELs) [1–3] have the advantage of high power, excellent beam quality and simple cavity designs allowing for tunable, single frequency operation, or passive modelocking by using a SESAM [4]. There is a strong commercial interest to advance this laser technology into the short-wave infrared (SWIR) and mid-IR spectral region [5–7]. In the 2-μm regime InGaSb based VECSELs have shown high-power cw operation [3,8–12]. However, reports on passive modelocking are limited to only low average output power of up to 25 mW to date [13–15].

Thermal management becomes more challenging for longer wavelength. Best results for cw and modelocked operation for 1-μm InGaAs VECSELs have been achieved with flip-chip processing and cooling from the backside [2,16] which is in contrast to the best results from InGaSb VECSELs to date [3,5–12]. So far at longer wavelength an intracavity heatspreader has been required which has several trade-offs. The highest thermally conducting material is diamond which is the material of choice for most heatspreaders. This is expensive, as intracavity diamonds of highest optical quality are difficult to produce. One key parameter is unwanted birefringence of diamond. Furthermore such an intracavity heatspreader requires a high-quality antireflection (AR) coating to reduce etalon effects and losses. For modelocking a broadband AR-coating and even a wedged heatspreader is often required introducing unwanted angle dispersion [8,12]. To the best of our knowledge the highest reported average output power for InGaSb flip-chip processed and backside-cooled VECSELs is 11.3 mW [17,18] limited by its thermal resistance

of $\geq 92\,\mathrm{K\,W^{-1}}$ [18]. This has been attributed to the poor thermal conductivity of GaSb-based materials in comparison to GaAs and the thicker layers of the GaSb-based DBR [3]. However, the bulk thermal conductivity material parameters alone cannot explain an increase from $2.5\,\mathrm{K\,W^{-1}}$ [19,20] to $92\,\mathrm{K\,W^{-1}}$ when changing the material system from GaAs to GaSb.

To overcome the current challenge to scale average power of passively modelocked InGaSb VECSELs a more detailed understanding of gain parameters is required which was previously demonstrated for InGaAs VECSELs in the near-infrared around $1\,\mu\mathrm{m}$ [21–23]. To date, for $2\text{-}\mu\mathrm{m}$ VECSEL, the understanding of the gain parameters heavily relies on simulations. These simulations often give limited insight since they focus on quantum structures or an isolated quantum well (QW) and therefore often ignore micro-resonator effects, temperature gradients or the integration of the QW that can potentially change the gain [24–29].

For the first time, we present the full gain characterization of any long-wavelength VECSEL and cw lasing results of backside-cooled InGaSb VECSEL emitting from $2020 - 2120\,\mathrm{nm}$. This VECSEL chip is compared to a commercially available VECSEL with an intracavity heatspreader for thermal management. Using two new characterization setups a detailed comparison of the gain parameters is performed. For the first time an InGaSb flip-chip processed and backside-cooled VECSEL performs similar to an intracavity heatspreader. Our chip shows a record low thermal resistance of only $3.45\,\mathrm{K\,W^{-1}}$ (comparable to near-infrared InGaAs VECSEL chips) and generates an average output power of more than $800\,\mathrm{mW}$ with only a 0.5% output coupler.

2. Novel structure design and gain characterization experiments

Table 1 compares the structures of the two VECSEL chips used in this work. Both structures are grown with MBE, structure 1 is commercially available and structure 2 was grown at our clean room facility FIRST at ETH Zurich. Structure 1 is a commercial InGaSb VECSEL chip with a wedged, AR-coated, intracavity diamond for heat removal from the active region. We estimate the AR coating to reflect $\sim 0.1\%$ of the laser mode by measuring the power of a second output beam coming from the wedged surface. Structure 2 is our own InGaSb VECSEL chip flip-chip processed and cooled from the backside only. For the details of the semiconductor processing we refer to the Methods section.

Table 1. InGaSb VECSEL gain chips with two different heat management and different designs. Structure 2 was optimized for passive modelocking with an antiresonant field intensity enhancement and backside cooling with similar average output power in comparison to a commercial more resonant device with an intracavity heatspreader (structure 1).

VECSEL gain chip	structure 1	structure 2
growth	MBE, VEXLUM	MBE, FIRST cleanroom ETH Zurich
heat management	intracavity diamond front side cooling	flip-chip processed back side cooling
active region	resonant	antiresonant
field intensity enhancement	~ 2	1.2
anti-reflection section	AR coated, wedged diamond	PECVD Si_3N_4
maximum cw power	985 mW @ 17 °C	812 mW @ −10 °C
lasing wavelength	2044 ± 10 nm	2080 ± 40 nm

2.1. InGaSb VECSEL chip structure 2 optimized for passive modelocking

Figure 1(a) shows the antiresonant InGaSb VECSEL chip design of structure 2. On top of a 19-pair DBR (GaSb/AlAs$_{0.08}$Sb$_{0.92}$ layers) the active region has $5\times 3\, In_{0.27}Ga_{0.73}$Sb QWs placed

in the antinodes of the incoming lasing beam in a linear standing-wave cavity. The active region consists of $AlAs_{0.08}Sb_{0.92}$ barrier layers around the gain QW to increase the PL with a shorter carrier capture rate into the QW. This is determined by carrier diffusion through the pumped barriers and the relaxation rate into the QW [23]. The last layer is PECVD grown Si_3N_4 and serves as an AR coating, helping the laser mode to be transmitted to the active region. For higher average power with modelocking it is beneficial to operate at antiresonance with a lower gain saturation [30,31].
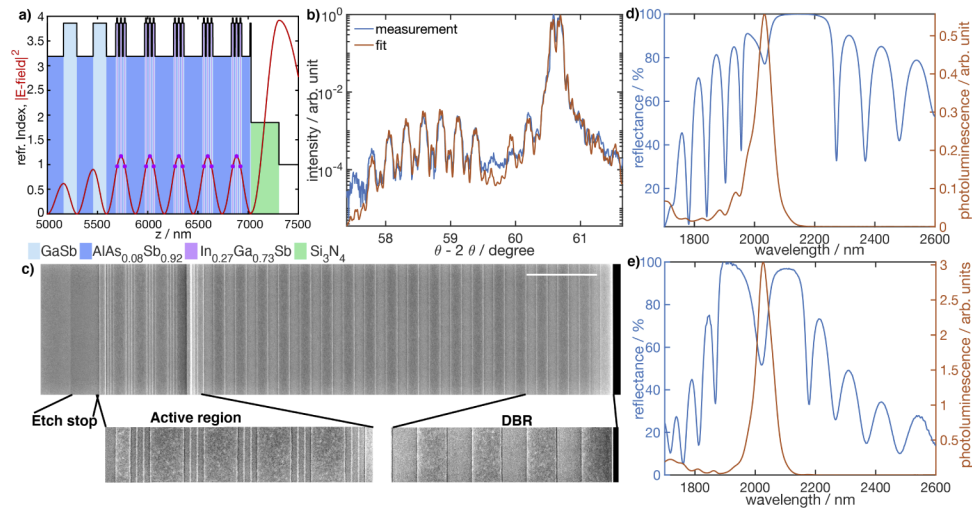
Fig. 1. InGaSb VECSEL chip design and standard characterization. a) Design of structure 2 with the 15 $In_{0.27}Ga_{0.73}Sb$ gain quantum wells (QWs) placed in 5 antinodes of the standing wave intensity pattern. Red line shows the field intensity enhancement which is 4 for a 100% reflector and 1.2 at the gain QWs for our antiresonant design. b) XRD analysis of the as-grown structure 2. A fit is shown in red. c) SEM image of structure 2. The different regions of the VECSEL chip are indicated and shown zoomed in. The scalebar is 1 μm. d) Measured linear reflectance and PL of the processed structure 2. e) Measured reflectance and PL for structure 1 without the intracavity heatspreader.

In Fig. 1(b) an x-ray diffraction (XRD) analysis of the as-grown chip is performed, showing monolithic growth quality with good interfaces. Since the gain QWs consist of ternary materials $In_{0.27}Ga_{0.73}Sb$ they are strained which can be seen from the side peaks at lower angles. The design is validated by SEM images of the cross-section in Fig. 1(c) which shows clear interfaces and the estimated thicknesses match with the design. Note this image is taken from the as-grown chip before processing, and therefore it shows the structure in reverse order and with an additional etch stop. The intermediate $AlAs_{0.08}Sb_{0.92}$ layers can be seen as white lines in the active region, the QWs do not show any contrast.

Structure 1 is a commercial, high-power VECSEL chip, bonded to a wedged, AR coated 0.3 mm thick diamond heatspreader. The diamond not only allows for efficient cooling but also increases the field intensity enhancement in the QW region (see Table 1) by reducing the refractive index contrast to the semiconductor.

Figure 1(d) and (e) show the measured wavelength-dependent linear reflectance and photoluminescence (PL). In structure 1 (Fig. 1(e) this is performed without the intracavity heatspreader and for structure 2 (Fig. 1(d) with the fully flip-chip processed chip. Both structures show a typical DBR spectral reflectance with a high reflecting part i.e. stop-band. In the stop-band the absorption dip of the QWs is located. For structure 1, the QW absorption dip is more pronounced and the PL is higher because of its more resonant structure design. Note, that the QW absorption

dip for structure 2 is on the blue edge of the stop-band to take into account a stronger heating of the pumped VECSEL chip when cooled from the backside. This heating leads to a redshift of the QW's bandgap by $1.3\,\mathrm{nm\,K^{-1}}$ and therefore of the lasing emission.

2.2. Gain characterization

Here we introduce and demonstrate an optical characterization for a wavelength range of 1.9 to $3\,\mu\mathrm{m}$ to precisely measure wavelength-dependent gain saturation and spectral gain. We adapt this characterization from the near-IR result [22] as shown in Fig. 2, which however is significantly more challenging in the long-wavelength regime with the demonstrated accuracy of <0.015% in gain saturation and 0.1% in spectral gain around $2\,\mu\mathrm{m}$.
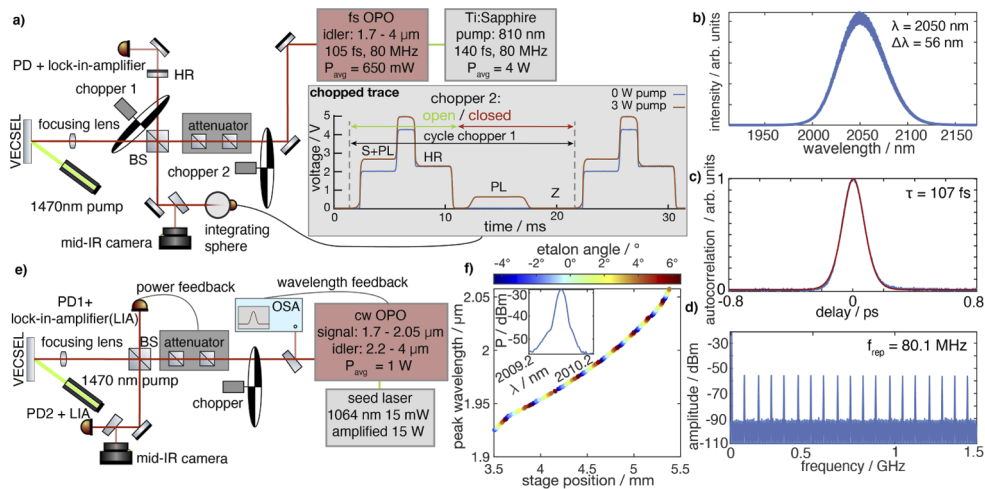
Fig. 2. Nonlinear and wavelength-dependent gain characterization covering a wavelength range of 1.9 to $3\,\mu\mathrm{m}$. a) Gain saturation setup. b)-d) Femtosecond OPO with the optical spectrum b) having a FWHM of 56 nm, the autocorrelation showing a pulse width of 107 fs and the microwave spectrum in d) with a repetition rate of 80.1 MHz. e) Spectral gain setup. f) Wavelength tuning for the cw OPO and a spectrum in the inset. We demonstrate an accuracy of <0.015% in gain saturation (over more than 3 orders of magnitude) and 0.1% in spectral gain around $2\,\mu\mathrm{m}$. BS: beamsplitter

A commercial broadband, femtosecond OPO (Radiantis Oria IR XT) is used as the probe laser for the gain-saturation measurements. It is pumped by a femtosecond Chameleon Ultra Ti:sapphire laser operating at 810 nm as shown in Fig. 2(a). The OPO's idler beam can be tuned from $1.7 - 4\,\mu\mathrm{m}$ with 107 fs pulse duration at a repetition rate of 80.1 MHz and a maximum average output power of 650 mW. Figure 2 b-d) display the typical pulse characterization consisting of the optical spectrum, the autocorrelation trace and the microwave spectrum. The calculated time-bandwidth product is 1.36 times the one of an ideal hyperbolic secant square pulse. After entering the setup, the beam is attenuated with two wire-grid polarizers where one is placed on a motorized rotation stage. The wire-grid polarizers are very broadband and show no beam pointing variations with rotation. Afterwards the beam is split to a device under test (DUT) and a reference arm. The reference arm is terminated with an HR that has a known reflectance. The leakage through this mirror is guided to a photodiode to monitor the fluence. The VECSEL chip is the DUT. The DUT arm uses a focusing lens to reach higher fluences on the DUT. The DUT is probed under an incident angle of 0° so that the reflection is collected with the same lens. The pump comes from the side (shown in green) under an incident angle of 30°. Both beams are recombined at the beamsplitter and guided to an integrating sphere photodiode to measure the

reflectance. The two choppers are tightly phase locked with a finer outer wheel and chopper 2 is run at half the frequency of chopper 1 allowing to block the beam in every second cycle of chopper 1. The photodiode is amplified with a dynamic-gain current amplifier. An adaptive integration keeps the measurement time and noise level low at the same time. A typical trace is shown next to the setup where the chopper cycles and levels are indicated. This corrects for spontaneous emission i.e. PL from the gain chip. Employing broadband optics the setup operates from 1.9 μm to beyond 3 μm.

Before a measurement the absolute fluence is calibrated by measuring the maximum power and the probe spot size with a scanning slit profiler. A test measurement replacing the DUT with a calibrated HR is performed to exclude for any nonlinearities in the setup. A microbolometer based mid-IR camera helps aligning the DUT and placing it in the focus by comparing the beam sizes from reference and DUT arm and their respective position.

For the spectral gain setup in Fig. 2(e) a commercial tunable cw-OPO with a signal from 1.7 to 2.05 μm and an idler from 2.2 to 4 μm is used. Automated wavelength tuning with a feedback loop is performed by changing the OPO's nonlinear-crystal position and an etalon angle in the OPO cavity for fine tuning. Figure 2(f) shows the OPO-signal tuning curve at different positions and etalon angles giving single mode emission at highest output power. A typical spectrum in the inset shows that the linewidth of the OPO-signal is below the resolution of the OSA. The OPO's signal beam can be tuned from $1.7 - 2.05$ μm and the idler beam from $2.2 - 4$ μm. The beam is guided into the setup shown in Fig. 2(e). A small part of the beam is guided to an OSA giving feedback to the wavelength tuning. Afterwards the main beam is chopped. After attenuating and splitting the beam in the same way as in the setup before, the reference beam is directly guided onto a photodiode (PD1). This photodiode gives a reference level and provides power feedback to maintain a constant power of 0.7 mW on the DUT for each wavelength. In the DUT arm the beam is focused to get a spot size comparable to a laser intracavity mode size. The pump is the same as in the previous setup. In this setup only the DUT beam is going back to the beamsplitter and is then detected on PD2. The two photodiode signals are compared using a lock-in amplifier which removes the unchopped PL. To avoid any interference of the highly coherent cw-OPO signal, we use a pellicle beamsplitter, all other optics and photodiodes are slightly tilted and all reflections are carefully dumped [21].

3. Results and discussion

Here we report the cw lasing result from the two optically pumped VECSELs (see Table 1) with a linear straight laser cavity. In addition we first present the full gain characterization results. Note that the VECSEL gain chip has both one highly reflective cavity end mirror and the active region fully integrated within one chip and therefore a reflectance above 100% corresponds to gain.

3.1. Gain saturation

Figure 3(a) shows the gain saturation measurements of structure 1 at different pump powers. The measurements are performed at a center wavelength of 2040 nm and 17 °C. At low pump power the behavior is similar to a SESAM with increasing reflectance for higher fluences [32]. At very high fluences inverse saturable absorption decreases the reflectance in the rollover [33]. The experimental data is fitted with an empirical model that is established for 1-μm VECSEL [22]

$$R^{\text{FlatTop}}(F) = R_{\text{ns}} \frac{F_{\text{sat}}}{F} \ln \left[1 + \exp \left(\frac{R_{\text{ss}}}{R_{\text{ns}}} \right) \left(\exp \left(\frac{F}{F_{\text{sat}}} \right) - 1 \right) \right] \exp \left(-\frac{F}{F_2} \right) \tag{1}$$

$$R^{\text{Gauss}}(F) = \int_0^1 \mathrm{d}z \, R^{\text{FlatTop}}(2Fz). \tag{2}$$

The obtained fit parameters in Eq. (1) are interpreted as small signal gain $g_{\text{ss}} = R_{\text{ss}} - 100\%$, nonsaturable losses $\Delta R_{\text{ns}} = 100\% - R_{\text{ns}}$, saturation fluence F_{sat} and inverse saturable absorption

parameter F_2. The adapted weighting in Eq. (2) allows to apply this model to a Gaussian beam. The calibrated HR measurement shown in grey demonstrates an accuracy <0.015% of the setup over the full fluence range of more than 3 orders of magnitude. At high pump powers the small signal gain saturates at higher fluences typical for VECSEL structures.
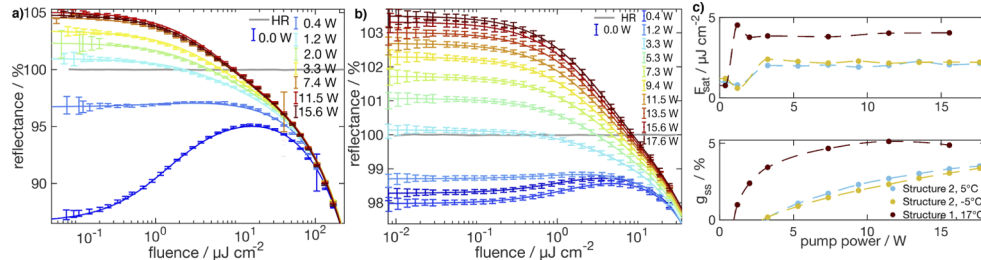
Fig. 3. Gain saturation measurements. Measurement of pump-power-dependent gain saturation of a) structure 1 and b) structure 2. The 99.99% HR is shown in grey. The probe fluence is varied over 3.5 orders of magnitude. c) Measured pump-power-dependent saturation fluence and small signal gain for both chips.

Figure 3(b) displays the same measurements for structure 2 performed at 2070 nm and 5 °C. The initial modulation depth of the SESAM-like behavior is less prominent because the structure's bandgap is detuned with no pump-heating present.

Figure 3(c) compares the pump power dependent fit parameters for both chips and different temperatures. Neither the saturation fluence nor the small signal gain strongly depend on temperature. The saturation fluences are low at small pump powers and jump to a higher, constant value as soon as the gain region is reached above 100%. Structure 1 shows double the saturation fluence compared to structure 2. Also, the small signal gain increases more sharply and to higher values for structure 1 because the structure is directly at the designed working temperature of 17 °C.

3.2. Spectral gain

Figure 4(a) shows the spectral gain measurements for structure 1 at 17 °C. With increasing pump power the absorption dip within the stop-band becomes smaller until the probe beam experiences more than 100% reflectance and therefore increasing small signal gain. A calibrated HR measurement is shown in grey. The maximum small signal gain is more than 5% and a gain bandwidth of more than 80 nm FWHM is reached.

These spectral gain measurements are compared to simulations with the designed gain structures. To apply the quantum mechanical gain properties quantitatively to a VECSEL device, material properties are linked to a real micro-resonator device geometry which predicts spectral gain as measured in VECSEL structures. The grown structure is reconstructed in a transfer matrix simulation tool, the QW properties are calculated in next**nano**++ and for the pump absorption a bleached absorption model is developed. A simulation of the spectral gain is performed in Fig. 4(b) with the detailed procedure described in the Methods section. Both simulation and experiment match well for different pump powers in terms of shape and peak small signal gain. The simulated gain bandwidth is slightly lower, since the simulation is performed at constant temperature neglecting any temperature gradients in the structure. Figure 4(c) shows the spectral gain measurements of structure 2 at −20 °C. The behavior is similar to structure 1 but due to a higher heating the redshift of the spectral gain measurements is more pronounced. Also this structure yields a maximum small signal gain of more than 5% and the estimated gain bandwidth is even larger than 100 nm. Figure 4(d) shows again a simulation of the spectral gain that reproduces the expected behavior. Nevertheless, the gain looks much narrower in the simulation.
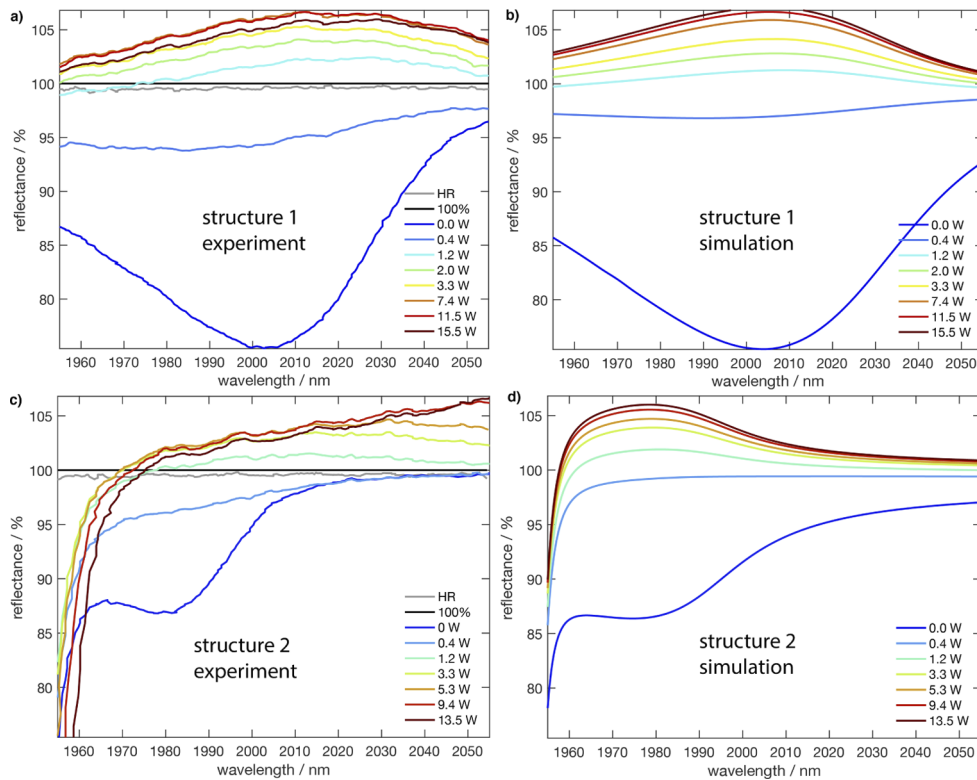
Fig. 4. Spectral gain. a,b) Structure 1 and c,d) Structure 2. a,c) are pump-power-dependent measurements obtained with a probe power of 0.7 mW and a spot size of 80 µm diameter. The pump has a spot size of 430 µm. The grey line is a 99.5% HR and the gain region is separated by a black 100% line. b,d) Simulations for chips with the same geometry.

This happens because no heating effects are considered in the simulation which puts the emission at the edge of the stop-band. Moreover, the temperature gradient in both the lateral as well as transversal direction increases the gain bandwidth even further for structure 2.

By integrating the quantum simulations from next**nano**++ in a transfer matrix method, it is possible to make predictions for the reflectance under pumped conditions. The quasi Fermi-levels are computed self-consistently by using a model for a bleached pump absorption and passing on the quasi-Fermi levels to the QWs. This links material properties obtained from quantum mechanics to a real micro-resonator device geometry and therefore allows for spectral-gain prediction as it is measured from VECSEL structures. The spectral-gain measurements show high small signal gain and even a broader gain bandwidthVECSEL than expected from the simulations. Therefore both are suitable for laser operation which is compared in the next paragraph.

3.3. Laser operation

It is well-known that an intracavity heatspreader provides better heat management. Here we show that we can obtain sufficient cw lasing performance when we adjust the heatsink temperatures accordingly. A cw test cavity compares the lasing performance. The linear straight laser cavity uses a 0.5% output coupler with a 100 mm radius of curvature with a cavity length of 60 mm. The VECSEL chip is mounted on a peltier element for temperature control. The straight cavity allows for pumping under 30° angle. The pump spot has 400 µm diameter. This setup automatically measures output power, reflected pump power, spectra and beam profiles as a function of pump

power and peltier temperature T. With this it is possible to calculate the thermal resistance via the spectral shift in dependence of pump power and temperature [17]

$$R_{\text{th}} = \frac{\Delta\lambda}{\Delta P_{\text{pump}}} \left(\frac{\Delta\lambda}{\Delta T}\right)^{-1} . \tag{3}$$

Figure 5(a) and (b) summarize the results obtained from the cw test cavity. Fig. 5(a) shows the power slopes of structure 1 at different temperatures above the dew point. Output powers >800 mW are reached. With increasing temperature the output power decreases showing a typical efficiency decrease of semiconductor lasers. Both VECSEL chips have no pump DBR and therefore a significant amount of pump light is absorbed in places not useful for lasing as for example in the GaSb layers of the DBR. In addition, for both VECSELs we measured less than 10% reflected pump power. Therefore, we only refer to output power vs. pump power and the slope-efficiencies would be much higher with a pump DBR. The spectrum in the inset indicates single mode behavior and the output beam is Gaussian shaped indicating a good beam quality. Both spectrum and beam profile are recorded at the linear range of the power slope. Figure 5(b) shows similar power slopes for structure 2. Also here output powers >800 mW are reached at similar pump power even though operation temperatures need to be lower. The beam profile is comparable but the spectrum is broader. This is due to the temperature gradient in the structure. Using these measurements together with Eq. (3) the thermal resistance for both chips is calculated. Whereas the intracavity heatspreader reaches a thermal resistance of $1\,\text{K W}^{-1}$, the flip-chip processed structure has a thermal resistance of $3.5\,\text{K W}^{-1}$. This is the lowest value reported of any flip-chip processed backside-cooled InGaSb VECSEL chip without an intracavity heatspreader. These values are both in a good range even when compared to standard flip-chip processed 1-µm InGaAs VECSELs which give a value of $2.5\,\text{K W}^{-1}$ [19,20]. The origin of this big improvements has two main reasons. Because of the pump spot size we theoretically expect the thermal resistsance to drop to some value around $12\,\text{K W}^{-1}$ [18]. The other improvement we attribute to an improved growth and processing quality.

Figure 5(c) compares the spectral shift of both structures taken from spectral gain measurements at different heatsink temperatures with a linear fit which confirm the lower thermal resistance of structure 1. Figure 5(d) compares the gain bandwidth of both structures taken from spectral gain measurements at different heatsink temperatures. The values represent FWHM bandwidth obtained from fitting a Gaussian function to the gain region >100%. Resonant structure 1 has a maximum gain bandwidth of 90 nm whereas structure 2 reaches values of 120 nm. This has two reasons: First, structure 2 is an antiresonant design designed for a lower field intensity enhancement in the gain quantum well which leads to a broader absorption and gain bandwidth. Second, structure 2 has a higher thermal resistance with a larger temperature difference in lateral direction which leads to different gain wavelengths. Moreover, the temperature gradient in transversal direction increases this effect even further. Figure 5(e) shows for structure 2 the temperature-dependent small signal gain from gain saturation measurements at a fixed wavelength. This shows a clear maximum where the heatsink temperature matches best lasing performance. Moreover, the temperature-dependent slope efficiency is shown with a linear fit. The slope efficiency decreases with temperatures having a maximum value of 8.5% which is competitive for 2-µm lasers [3]. Note, at this point no pump DBR has been used.

Table 2 summarizes the gain parameters for both structures taken from the different experiments.

Structure 1 has a higher saturation fluence. Structure 1 also has a higher maximum small signal gain in the gain saturation measurements which is due to the fact that structure 2 heats up more which redshifts the optimal emission when increasing the pump power. However, structure 2 has a higher induced absorption parameter. This is probably the case because the active region contains $AlAs_{0.08}Sb_{0.92}$ between the quantum barriers which does not show two-photon absorption at the lasing wavelength. Moreover, the nonsaturable losses of structure 2 are much smaller. This
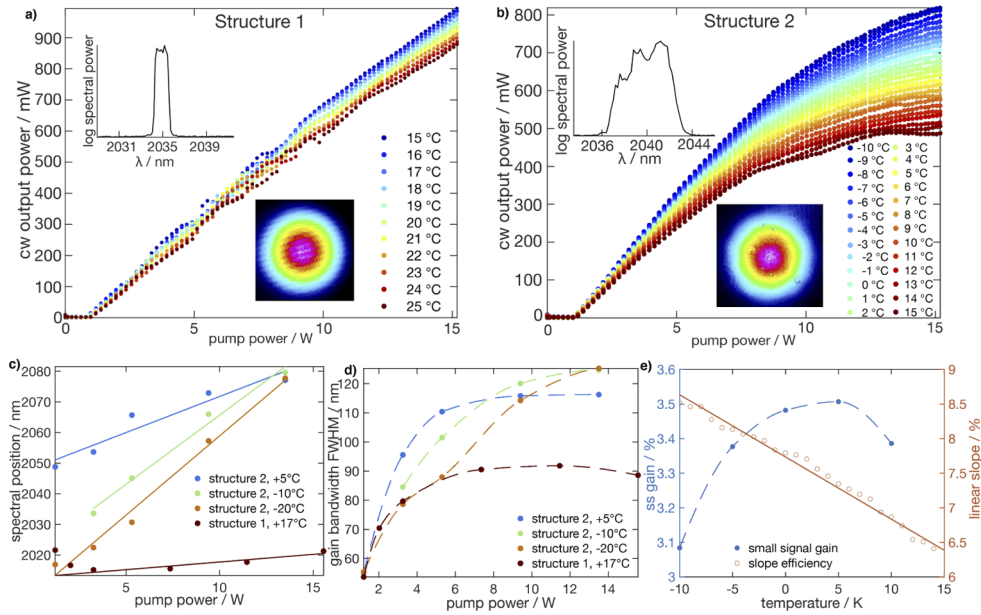
Fig. 5. Optically pumped VECSELs with intracavity heatspreader (structure 1) and with backside cooling (structure 2) as a function of pump power and heatsink temperature: a) (b)) average cw output power for structure 1 (structure 2). The insets show an exemplary optical spectrum and beam profile. Spectral gain from spectral gain measurements shown in Fig. 4: c) spectral shift, and d) gain bandwidth. e) Structure 2 small signal gain as a function of heatsink temperature at a fixed pump power of 15 W extracted from gain saturation measurement shown in Fig. 3 and the slope efficiency linear region taken from the power slopes shown in b). It is clear that an intracavity heatspreader provides better heat management, but sufficient performance can be achieved with backside cooling.

Table 2. The gain parameters for both VECSEL chip structures are shown. The experiments from which these parameters are derived are shown in bold font. ISA: induced saturable absoprtion

VECSEL gain chip	structure 1 at 17 °C	structure 2 at 5 °C
gain saturation		
saturation fluence F_{sat} / μJ cm^{-2}	3.9 ± 0.13	2.06 ± 0.11
max. small signal gain g_{ss} / %	5.1	3.5
ISA fluence F_2 / mJ cm^{-2}	1.72 ± 0.034	2.01 ± 0.065
nonsaturable losses ΔR_{ns} / %	2.83 ± 0.15	0.98 ± 0.12
spectral gain		
peak small signal gain / %	6.5	5.9
max. gain bandwidth / nm	92	116
peak shift / nm W^{-1}	0.5	2.4
cw power slopes		
thermal resistance / K W^{-1}	1.07 ± 0.17	3.45 ± 0.53
optical-to-optical efficiency / %	7.4	7.4

is due to the fact that the wedged intracavity heatspreader introduces losses in the cavity. We estimate these losses to be 0.1% at the optimum wavelength by measuring the output power of the reflected beam from the wedged front surface of the heatspreader during lasing operation

and comparing it to the output coupling rate. Since the spectrum of the femtosecond OPO probe has a FWHM of 56 nm, also wavelengths less ideal for the heatspreader's AR coating are reflected. This leads to these high nonsaturable losses of 2.8%. Structure 2 also has a higher gain bandwidth allowing for a broader emission which is essential for short pulse generation. The higher peak shift of structure 2 is directly related to the higher thermal resistance that is still in a reasonable range even when compared to flip-chip processed, high quality 1-μm InGaAs VECSEL chips. The optical-to-optical efficiency is comparable which is due to the fact that the same pump-wavelength and similar QWs are used. These results clearly demonstrate that the flip-chip processed backside-cooled InGaSb VECSEL chips results in similar cw lasing performance when compared to the intracavity heatspreader-based heat management approach. This paves the way towards a new generation of cw and passively modelocked 2-μm VECSELs that are cheaper and solve the power scaling challenges.

4.   Conclusion and outlook

We have introduced and demonstrated two setups that precisely measure the gain saturation and spectral gain properties of optically pumped VECSEL chips for 1.9 μm to 3 μm. Gain characteristics are measured as a function of wavelength, fluence, pump power and heatsink temperature. For the nonlinear reflectance measurements we used around 100-fs pulses and for the spectral reflectance measurements a tunable cw-OPO. The setups measure the reflectance of an HR with a standard deviation of <0.015% for the gain saturation and <0.1% for the spectral gain. This is an excellent accuracy comparable to near-infrared VECSEL characterization. Theoretical simulations based on the 2-μm InGaSb VECSEL design structure are in very good agreement with these measurements which will help for further design optimizations at even longer wavelength.

Using these new gain characterization setups together with a cw test cavity the gain parameters of two 2-μm InGaSb VECSEL gain chips are compared using either intracavity or backside heatsinks. The intracavity heatsink provides superior heat management but with some trade-offs for passive modelocking applications. Adapting the heatsink temperatures for the two VECSELS we could obtain more than 800 mW cw output power. Moreover, they have small signal gains of more than 5%, small saturation fluences and gain bandwidths of more than 90 nm. The backside cooled, flip-chip processed structure is superior in terms of gain bandwidth and nonsaturable losses which is beneficial for passive modelocking.

For the first time a backside-cooled 2-μm-VECSEL was demonstrated with similar average output power as a VECSEL cooled with an intracavity heatspreader. We increased the average power to more than 800 mW, demonstrated reliable and precise gain characterization and obtained a very good agreement with theoretical predictions. Using these results combined with a SESAM [32] with low saturation fluence and low nonsaturable losses should enable passive modelocking at higher output powers.

5.   Methods

5.1.   Growth and processing

Growth is performed in an Veeco Gen III MBE. An Sb cracker with the cracking zone at 900 °C is used. Growth temperatures are 480 °C for the DBR and the active region. The As/Sb ratio is carefully adjusted to obtain lattice matching for the ternary materials $AlAs_{0.08}Sb_{0.92}$ and $InAs_{0.92}Sb_{0.08}$. A 2″ (001)-GaSb wafer with a thickness of 500 μm is used as a substrate. Growth is performed in reverse order starting with the $InAs_{0.92}Sb_{0.08}$ etch stop, followed by the active region and then the highly reflective DBR. 4.5×4.5 mm^2 pieces are cleaved after growth and then metalized with 20 nm Ti/ 30 nm Pt/ 5000 nm In/ 200 nm Au. The chips are pressed on a diamond heatspreader of 5×5 mm^2 that is metalized with 20 nm Ti/ 30 nm Pt/ 100 nm Au. In a

vacuum chamber with a pressure of $<5 \cdot 10^{-5}$ mbar, chip and heatspreader are gradually heated to 160 °C to form a bond. To minimize strain from different thermal expansion coefficients the cooling down is performed slowly over 30 min. Afterwards, the bonded structure is thinned down by 480 μm on substrate side with a Logitech PM5 lapper. Afterwards the other side is protected with wax on a polytetrafluoroethylene slide. The residual 20 μm of the GaSb substrate are removed with a solution mixture of 33% CrO_3 and 50% hydrofluric acid, diluted in water 1 : 5 [17]. The wet etching takes approximately 2 min and a clear, mirror-like surface on top of the 400 nm $InAs_{0.92}Sb_{0.08}$-etch stop layer remains with a selectivity of about 1 : 100 compared to GaSb. Subsequently, the etch stop is removed with a solution of citric acid and hydrogen peroxide which takes around 3 min and has a similar selectivity of 1 : 100 [34]. Again a mirror like surface on top of the VECSEL structure remains. The protective wax is removed by heating and trichloroethylene. This structure is coated with a single $\frac{\lambda}{4}$-layer of Si_3N_4 as an AR coating. For this, an Oxford Instruments PECVD Plasma Pro 80 at 120 °C base plate temperature is used. The chips are then soldered on a T-shaped copper mount that is then screwed on a Peltier cooled heatsink for optical characterization and lasing operation.

5.2. Standard characterization

SEM images are taken with a Zeiss Ultra 55 plus using the in-lens detector and an acceleration voltage of 10 kV. Before, SEM samples are cleaved freshly and are carefully mounted to have a clean interface. XRD measurements are performed with a Seiffert XRD 3003 PTS-HR and fitted. Linear reflectance measurements are performed on a Bruker VERTEX 80v FTIR using a globar light source and a liquid nitrogen cooled InSb detector. Attached to the FTIR is a PL unit with an excitation laser of 1064 nm. For all the measurements a 1470 nm DILAS pump diode is used giving 15 W. The beam profiles are recorded with a DataRay WinCamD-IR-BB. Optical spectra are recorded with a Yokogawa AQ6376 OSA using a resolution of 0.1 nm for the wavelength tuning and 1 nm for the tests in the laser cavity.

5.3. Spectral gain simulations

To compute the spectral gain the grown structure is reconstructed in a custom-developed, transfer matrix simulation tool for electric field distributions and reflection spectra using layer thicknesses from SEM measurements and all refractive indices from ellipsometer measurements with two exceptions:

1. the imaginary part of the refractive index (i.e. absorption) of the QW barrier material is bleached at high pump intensities.

2. the QW absorption or gain is calculated from quantum mechanical properties depending on the excitation.

We derive the gain depending on quantum mechanical properties like band structure, matrix elements and optical excitation [35–37]:

Starting with the Schrödinger equation, minimal coupling and a harmonic vector potential in dipole-approximation, one can find the harmonic, non-Hermitian perturbation Hamiltonian as

$$H' = \frac{eA_0}{2m_0} \boldsymbol{\epsilon} \cdot \hat{\mathbf{p}}, \tag{4}$$

where $\boldsymbol{\epsilon}$ is the unit vector in the polarization direction of the optical electric field, A_0 is the real amplitude of the vector potential, e (m_0) are charge (mass) of the electron and $\hat{\mathbf{p}}$ is the momentum operator. With the difference for absorbed and emitted photons Fermi's golden rule gives us the

emission rate between two levels a, b in terms of transition intensities $I_{ba}(\mathbf{k}) = \frac{2}{m_0} |\boldsymbol{\epsilon} \cdot \hat{\mathbf{p}}_{ba}|^2$ as

$$R_{ba}(\omega) = \frac{\pi e^2 A_0^2}{4 \hbar m_0} \frac{1}{V} \sum_{\mathbf{k}} I_{ba}(\mathbf{k}) \left[f_b(\mathbf{k}) - f_a(\mathbf{k}) \right] \delta(E_b(\mathbf{k}) - E_a(\mathbf{k}) - \hbar\omega). \tag{5}$$

The occupation functions of a band in quasi-thermal equilibrium is a quasi-Fermi distribution

$$f(E_a(\mathbf{k}), E_{\mathrm{F}}) = \frac{1}{1 + \exp\left(\frac{E_a(\mathbf{k}) - E_{\mathrm{F}}}{k_{\mathrm{B}} T}\right)}, \tag{6}$$

where E_{F} is the band's quasi-Fermi level, k_{B} the Boltzmann constant and T the temperature. Replacing the sum in Eq. (5) with the two dimensional integral via the rule $\sum_{\mathbf{k}} \rightarrow \frac{O}{(2\pi)^2} \int \mathrm{d}^2\mathbf{k}$ we cancel out the non-confined dimensions $\frac{V}{O} = \frac{d L_y L_z}{L_y L_z}$. Dividing by the injected photon number calculated from the time-averaged magnitude of the Poynting vector $S = \frac{n(\omega) c \epsilon_0 \omega^2 A_0^2}{2}$, the gain coefficient calculates as $g(\omega) = \frac{\sum_{a,b} R_{ba}(\omega)}{S/\hbar\omega}$. As the integral in $\mathbf{k}$-space is computed numerically we introduce a Dirac sequence $\delta(x) = \lim_{\Delta \rightarrow 0} \frac{1}{\pi} \frac{\Delta}{x^2 + \Delta^2}$ with an energy broadening factor $\Delta \approx 5 - 8\,\mathrm{meV} \ll k_{\mathrm{B}} T$. The spectral dependent gain is then calculated via

$$g(\hbar\omega) = g_0(\hbar\omega) \frac{1}{d} \sum_{a,b} \int \mathrm{d}^2\mathbf{k} \, I_{ba}(\mathbf{k}) \left[f_b(\mathbf{k}) - f_a(\mathbf{k}) \right] \frac{\Delta}{(E_b(\mathbf{k}) - E_a(\mathbf{k}) - \hbar\omega)^2 + \Delta^2}, \tag{7}$$

with the prefactor $g_0(\hbar\omega) = \frac{\hbar e^2}{8\pi^2 m_0 n(\omega) c \epsilon_0 \hbar\omega}$. Here, n is the refractive index, c the vacuum speed of light and ϵ_0 the vacuum permittivity. For this, the transition intensities and band structure have to be known. Note, that absorption α and gain g are only distinguished by a sign $\alpha(\hbar\omega) = -g(\hbar\omega)$.

Energy dispersion $E(\mathbf{k})$ and transition intensities $I_{ba}(\mathbf{k})$ of a single QW are calculated with the commercially available software next**nano**++ using the $8 \times 8 - \mathbf{k} \cdot \mathbf{p}$ method [37]. The software gives us access to the wavefunctions, optical transition intensities, band-structure, strain and possible coupling of quantum wells in heterostructures. In contrast to gain, absorption can be directly calculated in next**nano**++'s optics module, which is used as a validation for the developed integration algorithm. For our simulations, only one transition gives a significant contribution to the calculated gain spectra.

The calculation for bleaching quantum barrier layers uses the band-edges (E_{v} and E_{c}) and effective densities of state (D_{v} and D_{c}) from next**nano**++ and literature, respectively [38]. For every pump intensity Φ and each quantum barrier layer a nonlinear equation

$$\alpha(E_{\mathrm{F,v}}, E_{\mathrm{F,c}}) = \alpha_0 \left[f(E_{\mathrm{v}}, -E_{\mathrm{F,v}}) - f(E_{\mathrm{c}}, E_{\mathrm{F,c}}) \right] \tag{8}$$

$$E_{\mathrm{F,v}} = E_{\mathrm{F,v}}(n_0) \tag{9}$$

$$E_{\mathrm{F,c}} = E_{\mathrm{F,c}}(n_0) \tag{10}$$

is numerically solved for the absorption α. The argument $n_0 = \frac{\tau \Phi}{\hbar\omega} \alpha$ corresponds to the number of excited carriers in the barrier. The radiative lifetime τ is in the range of $100\,\mathrm{ns}$ and strongly temperature dependent. Equation (10) is calculated with a 2$^{\mathrm{nd}}$ order Joyce-Dixon approximation

$$E_{\mathrm{F,c}}(n_0) \approx E_{\mathrm{c}} + k_{\mathrm{B}} T \left[\ln\left(\frac{n_0}{D_{\mathrm{c}}}\right) + A_1 \frac{n_0}{D_{\mathrm{c}}} + A_2 \left(\frac{n_0}{D_{\mathrm{c}}}\right)^2 \right] \tag{11}$$

with $A_1 = \frac{1}{\sqrt{8}}$ and $A_2 = -4.95009 \cdot 10^{-3}$ [39]. The analogous function is used for the valence band. With Eq. (8) the pump absorption is modified with regard to the quasi-Fermi levels for holes and

electrons. This leads to a bleaching effect at the pump wavelength. Calculating consecutively layer by layer, the incident pump power reduces gradually. Additionally the presence of a QW in between the barrier layers reduces the pump power further because of the in-well absorption ($\approx 0.86\%$ per QW).

To finally calculate the spectral gain we still miss the quasi-Fermi level in the QW. For simplicity, the mean value of the barrier layers sitting right and left to the QW is used. Using separate levels for electrons and holes, spectral gain is calculated depending on the location of each QW. For this, Eq. (7) is integrated numerically over the two dimensional **k**-space. This determines the complex part of the refractive index $\kappa = \frac{\lambda\, g(\hbar\omega)}{4\pi}$, which is used in the transfer matrix method for calculating electrical fields and reflectance spectra. The indium concentration in the QW is fine-tuned to match the measured band-edge seen in the reflectance measurements at room temperature. The only adjustable parameter is the radiative lifetime.

Disclosures. The authors declare no conflicts of interest.

Data availability. Data underlying the results presented in this paper are not publicly available at this time but may be obtained from the authors upon reasonable request.

References

1. U. Keller and A. C. Tropper, "Passively modelocked surface-emitting semiconductor lasers," Phys. Rep. **429**(2), 67–120 (2006).
2. B. W. Tilma, M. Mangold, C. A. Zaugg, S. M. Link, D. Waldburger, A. Klenner, A. S. Mayer, E. Gini, M. Golling, and U. Keller, "Recent advances in ultrafast semiconductor disk lasers," (2015).
3. M. Guina, A. Rantamäki, and A. Härkönen, "Optically pumped VECSELs: Review of technology and progress," J. Phys. D: Appl. Phys. **50**(38), 383001 (2017).
4. U. Keller, K. J. Weingarten, F. X. Kärtner, D. Kopf, B. Braun, I. D. Jung, R. Fluck, C. Hönninger, N. Matuschek, and J. Aus Der Au, "Semiconductor saturable absorber mirrors (SESAM's) for femtosecond to nanosecond pulse generation in solid-state lasers," IEEE J. Sel. Top. Quantum Electron. **2**(3), 435–453 (1996).
5. N. Schulz, M. Rattunde, C. Ritzenthaler, B. Rösener, C. Manz, K. Köhler, J. Wagner, and U. Brauch, "Resonant optical in-well pumping of an (AlGaIn)(AsSb)-based vertical-external-cavity surface-emitting laser emitting at 2.35 μm," Appl. Phys. Lett. **91**(9), 091113 (2007).
6. B. Rösener, M. Rattunde, R. Moser, S. Kaspar, C. Manz, K. Köhler, and J. Wagner, "GaSb-based optically pumped semiconductor disk lasers emitting in the 2.0-2.8 μm wavelength range," Proc. SPIE **7578**, 75780X (2010).
7. B. Rösener, M. Rattunde, R. Moser, S. Kaspar, T. Töpper, C. Manz, K. Köhler, and J. Wagner, "Continuous-wave room-temperature operation of a 2.8 μm GaSb-based semiconductor disk laser," Opt. Lett. **36**(3), 319 (2011).
8. A. Härkönen, M. Guina, O. Okhotnikov, K. Rößner, M. Hümmer, T. Lehnhardt, M. Müller, A. Forchel, and M. Fischer, "1-W antimonide-based vertical external cavity surface emitting laser operating at 2-μm," Opt. Express **14**(14), 6479 (2006).
9. J.-M. Hopkins, N. Hempler, B. Rösener, N. Schulz, M. Rattunde, C. Manz, K. Köhler, J. Wagner, and D. Burns, "High-power, (AlGaIn)(AsSb) semiconductor disk laser at 2 μm," Opt. Lett. **33**(2), 201 (2008).
10. N. Hempler, J. M. Hopkins, A. Kemp, B. Rösener, M. Rattunde, J. Wagner, and D. Burns, "20W, quasi-cw GaSb-based semiconductor disk laser," in *Lasers, Sources and Related Photonic Devices, OSA Technical Digest Series (CD)*, (Optical Society of America, 2010), p. ATuA14.
11. P. Holl, M. Rattunde, S. Adler, S. Kaspar, W. Bronner, A. Bachle, R. Aidam, and J. Wagner, "Recent Advances in Power Scaling of GaSb-Based Semiconductor Disk Lasers," IEEE J. Sel. Top. Quantum Electron. **21**(6), 324–335 (2015).
12. P. Holl, M. Rattunde, S. Adler, A. Bächle, E. Diwo-Emmer, R. Aidam, and J. Wagner, "GaSb-Based 2.0 μm SDL with 17W output power at 20°C," Electron. Lett. **52**(21), 1794–1795 (2016).
13. A. Härkönen, J. Paajaste, S. Suomalainen, J.-P. Alanko, C. Grebing, R. Koskinen, G. Steinmeyer, and M. Guina, "Picosecond passively mode-locked GaSb-based semiconductor disk laser operating at 2μm," Opt. Lett. **35**(24), 4090 (2010).
14. A. Härkönen, C. Grebing, J. Paajaste, R. Koskinen, J. P. Alanko, S. Suomalainen, G. Steinmeyer, and M. Guina, "Modelocked GaSb disk laser producing 384fs pulses at 2m wavelength," Electron. Lett. **47**(7), 454–456 (2011).
15. M. Guina, A. Härkönen, J. Paajaste, J.-P. Alanko, S. Suomalainen, C. Grebing, and G. Steinmeyer, "Passively mode-locked GaSb-based VECSELs emitting sub-400-fs pulses at 2 μm," Proc. SPIE **8242**, 824204 (2012).
16. B. Heinen, T. L. Wang, M. Sparenberg, A. Weber, B. Kunert, J. Hader, S. W. Koch, J. V. Moloney, M. Koch, and W. Stolz, "106 W continuous-wave output power from vertical-external-cavity surface-emitting laser," Electron. Lett. **48**(9), 516–517 (2012).

17. J. P. Perez, A. Laurain, L. Cerutti, I. Sagnes, and A. Garnache, "Technologies for thermal management of mid-IR Sb-based surface emitting lasers," Semicond. Sci. Technol. **25**(4), 045021 (2010).

18. M. Devautour, A. Michon, G. Beaudoin, I. Sagnes, L. Cerutti, and A. Garnache, "Thermal management for high-power single-frequency tunable diode-pumped VECSEL emitting in the near- and mid-IR," IEEE J. Sel. Top. Quantum Electron. **19**(4), 1701108 (2013).

19. E. J. Saarinen, K. Lahtonen, M. Valden, and O. G. Okhotnikov, "High power semiconductor disk laser with a semiconductor-dielectric-metal compound mirror," Appl. Phys. Lett. **104**(10), 101110 (2014).

20. K. Gbele, A. Laurain, J. Hader, W. Stolz, and J. V. Moloney, "Design and Fabrication of Hybrid Metal Semiconductor Mirror for High-Power VECSEL," IEEE Photonics Technol. Lett. **28**(7), 732–735 (2016).

21. C. Borgentun, J. Bengtsson, and A. Larsson, "Direct measurement of the spectral reflectance of OP-SDL gain elements under optical pumping," Opt. Express **19**(18), 16890 (2011).

22. M. Mangold, V. J. Wittwer, O. D. Sieber, M. Hoffmann, I. L. Krestnikov, D. A. Livshits, M. Golling, T. Südmeyer, and U. Keller, "VECSEL gain characterization," Opt. Express **20**(4), 4136 (2012).

23. C. G. E. Alfieri, D. Waldburger, E. Gini, G. Eisenstein, M. Golling, S. M. Link, and U. Keller, "Optical efficiency and gain dynamics of modelocked semiconductor disk lasers," Opt. Express **25**(6), 6402–6420 (2017).

24. W. Chow, M. Kira, and S. W. Koch, "Microscopic theory of optical nonlinearities and spontaneous emission lifetime in group-III nitride quantum wells," Phys. Rev. B **60**(3), 1947–1952 (1999).

25. J. Hader, S. W. Koch, and J. V. Moloney, "Microscopic theory of gain and spontaneous emission in GaInNAs laser material," Solid-State Electron. **47**(3), 513–521 (2003).

26. A. Thränhardt, S. W. Koch, J. Hader, and J. V. Moloney, "Carrier dynamics in quantum well lasers," Opt. Quantum Electron. **38**(4-6), 361–368 (2006).

27. C. Bückers, A. Thränhardt, S. W. Koch, M. Rattunde, N. Schulz, J. Wagner, J. Hader, and J. V. Moloney, "Microscopic calculation and measurement of the laser gain in a (GaIn)Sb quantum well structure," Appl. Phys. Lett. **92**(7), 071107 (2008).

28. C. Bückers, S. Imhof, A. Thränhardt, J. Hader, J. V. Moloney, and S. W. Koch, "Microscopic modeling of quantum well gain media for VECSEL applications," IEEE J. Sel. Top. Quantum Electron. **15**(3), 984–992 (2009).

29. I. Kilen, S. W. Koch, J. Hader, and J. V. Moloney, "Mode-locking in vertical external-cavity surface-emitting lasers with type-II quantum-well configurations," Appl. Phys. Lett. **114**(25), 252102 (2019).

30. O. D. Sieber, M. Hoffmann, V. J. Wittwer, M. Mangold, M. Golling, B. W. Tilma, T. Südmeyer, and U. Keller, "Experimentally verified pulse formation model for high-power femtosecond VECSELs," Appl. Phys. B: Lasers Opt. **113**(1), 133–145 (2013).

31. C. G. E. Alfieri, D. Waldburger, J. Nürnberg, M. Golling, and U. Keller, "Sub-150-fs pulses from an optically pumped broadband modelocked integrated external-cavity surface emitting laser," Opt. Lett. **44**(1), 25 (2019).

32. J. Heidrich, M. Gaulke, B. O. Alaydin, M. Golling, A. Barh, and U. Keller, "Full optical SESAM characterization methods in the 1.9 to 3-μm wavelength regime," Opt. Express **29**(5), 6647 (2021).

33. R. Grange, M. Haiml, R. Paschotta, G. J. Spühler, L. Krainer, M. Golling, O. Ostinelli, and U. Keller, "New regime of inverse saturable absorption for self-stabilizing passively mode-locked lasers," Appl. Phys. B: Lasers Opt. **80**(2), 151–158 (2005).

34. O. Dier, L. Lin Chun, M. Grau, and M. C. Amann, "Selective and non-selective wet-chemical etchants for GaSb-based materials," Semicond. Sci. Technol. **19**(11), 1250–1253 (2004).

35. C. S. Chang, S. L. Chuang, J. R. Minch, W. C. W. Fang, Y. K. Chen, and T. Tanbun-Ek, "Amplified Spontaneous Emission Spectroscopy in Strained Quantum-Well Lasers," IEEE J. Sel. Top. Quantum Electron. **1**(4), 1100–1107 (1995).

36. C. Ghezzi, R. Magnanini, A. Parisini, B. Rotelli, L. Tarricone, A. Bosacchi, and S. Franchi, "Optical absorption near the fundamental absorption edge in GaSb," Phys. Rev. B **52**(3), 1463–1466 (1995).

37. S. Birner, T. Zibold, T. Andlauer, T. Kubis, M. Sabathil, A. Trellakis, and P. Vogl, "Nextnano: General purpose 3-D simulations," IEEE Trans. Electron Devices **54**(9), 2137–2142 (2007).

38. I. Vurgaftman, J. R. Meyer, and L. R. Ram-Mohan, "Band parameters for III-V compound semiconductors and their alloys," J. Appl. Phys. **89**(11), 5815–5875 (2001).

39. L. A. Coldren, S. W. Corzine, and M. L. Mašanović, "Appendix Two: Relationships between Fermi Energy and Carrier Density and Leakage," in *Diode Lasers and Photonic Integrated Circuits*, (John Wiley & Sons Inc., 2012), pp. 529–544.